Chemical Engineering Journal 519 (2025) 164989

Contents lists available at ScienceDirect

Chemical Engineering Journal

journal homepage: www.elsevier.com/locate/cej

Edge-electron induced ferrimagnetic effect to accelerate interfacial desolvation kinetics toward dendrite-free Zn metal batteries

Haifeng Yang [a,b,1], Fangqi Liu [c,1], Bixian Chen [a,b,1], Xiaomin Cheng [a], Qinghua Guan [a], Jing Dong [a], Teng Li [b], Lujie Jia [a], Wenbin Wang [a], Jing Zhang [d], Jiqiang Jia [d], Yongzheng Zhang [e], Canhuang Li [f], Yunjian Liu [b,*], Hongzhen Lin [a,*], Jian Wang [g,h,**]

[a] i-Lab & CAS Key Laboratory of Nanophotonic Materials and Devices, Suzhou Institute of Nano-Tech and Nano-Bionics, Chinese Academy of Sciences, Suzhou 215123, China
[b] School of Materials Science and Engineering, Jiangsu University, Zhenjiang 212013, China
[c] Key Laboratory of Artificial Micro- and Nano-structures of Ministry of Education, School of Physics and Technology, Wuhan University, Wuhan 430072, China
[d] Advanced Materials Analysis and Test Center, School of Materials Science and Engineering, Xi'an University of Technology, Xi'an 710048, China
[e] State Key Laboratory of Chemical Engineering, East China University of Science and Technology, Shanghai 200237, China
[f] Catalonia Institute for Energy Research-IREC Department of Chemistry University of Barcelona, Barcelona 08028, Spain
[g] Helmholtz Institute Ulm (HIU), Ulm D89081, Germany
[h] Karlsruhe Institute of Technology (KIT), Karlsruhe D76021, Germany

ARTICLE INFO

Keywords:
Zinc metal batteries
Delocalized electron
Ferrimagnetic interphase
Catalytical desolvation
Self-motivated behaviors

ABSTRACT

Rechargeable aqueous zinc metal batteries (AZMBs) have garnered significant attention for large-scale energy storage. However, they are hindered by the sluggish $Zn(H_2O)_6^{2+}$ desolvation kinetics, leading to uneven Zn deposition as well as side reactions of active water molecules for the formation of hydrogen evolution reaction (HER). Herein, high spin-state ferrimagnetic interphase of spinel zinc ferrite (ZFO) has been pioneered to serve as artificial interphase on metallic Zn anode (ZFO@Zn). Specifically, high-spin Fe^{3+} center enhances electron delocalization and the spinel crystal structure of ZFO layer facilitates the interfacial ion transfers, catalytically reducing the barriers of Zn^{2+} desolvation and atom diffusion. Meanwhile, the micro-magnetic field self-motivates interfacial ion flux and separates the active molecules, enabling uniform Zn deposition without HER. The as-fabricated cell employed with ZFO@Zn achieved an impressive cumulative capacity exceeding 3500 mAh cm^{-2} at 30 mA cm^{-2}, demonstrating its remarkable kinetics and stability. The assembled vanadium-based full cell exhibits superior performance of 411.1 mAh g^{-1} at 10 A g^{-1} and maintained the capacity-retention of 90.7% after 3000 cycles at 5 A g^{-1}. Impressively, the large-areal pouch cell with ZFO@Zn anode stabilizes for 150 cycles, underscoring the potential of magnetic spinel materials for the commercialization of AZMBs.

1. Introduction

With the evolution of global energy landscape, the topics of resource sustainability and environmental protection of batteries are constantly mentioned. Among them, aqueous zinc metal batteries (AZMBs) are particularly promising for large-scale energy storage systems due to their high theoretical capacity (820 mAh g^{-1}, 5855 mAh cm^{-3}), low redox potential (−0.76 V vs. standard hydrogen electrode), and abundant resources of zinc [1]. Unlike lithium-ion batteries with high risks of combustion and high costs, AZMBs offer intrinsic safety and affordability owing to the application of safe aqueous electrolytes, making them an attractive choice for future grid-storage [2]. Despite above advantages, the metallic Zn anode still faces critical challenges, including hydrogen evolution reactions (HER), surface corrosion, and Zn dendrite growth. In principle, these issues stem from the bulky solvation shell of $[Zn(H_2O)_6]^{2+}$ clusters and it imposes significant steric hindrance to diffusion, leading to substantial desolvation energy barrier for successive reactions [3–5]. Additionally, the dissociation of active water molecules from the solvation shell exacerbates side reactions once the molecules reach electric contact.

* Corresponding authors.
** Correspondence to: J. Wang, Karlsruhe Institute of Technology (KIT), Karlsruhe D76021, Germany.
E-mail addresses: lyjian122331@ujs.edu.cn (Y. Liu), hzlin2010@sinano.ac.cn (H. Lin), jian.wang@kit.edu (J. Wang).
[1] H. Yang, F. Liu and B. Chen contributed equally to this work.

https://doi.org/10.1016/j.cej.2025.164989
Received 17 March 2025; Received in revised form 23 May 2025; Accepted 15 June 2025
Available online 19 June 2025

To address these challenges, significant research efforts have focused on electrolyte engineering or interface modification. For example, electrolyte engineering such as the introduction of organic additives or high-concentration salts can modify Zn^{2+} coordination environments and suppress potential HER with crowded water molecules in the electrolytes [6]. However, these approaches always undermine the high ionic conductivity of aqueous electrolytes, induce severe corrosion toward current collectors, and burden costs, which are contradictory to the goal of AZMBs for affordability. Another promising approach is the construction of artificial solid electrolyte interphase (SEI) layer, which chemically modulates the ion distribution and physically shields electrons from aqueous electrolytes [7]. Compared to self-generated SEI layers, artificial SEI layers feature tunable properties and uniform formation [8]. Nevertheless, existing designs still struggle to support rapid ion transport under high charge-discharge rates and prevent dendrite growth during prolonged cycling [9]. The development of a multi-step regulated artificial SEI layer for achieving long-term dendrite-free Zn plating/stripping with high reversibility remains an open problem.

Magnetic materials have shown potential in battery applications. For instance, Zhou et al. used magnetic Co_3O_4 nanocrystals to stabilize lithium metal anode, where the self-generated micro-magnetic field can simultaneously induce compact and deep Li deposition [10]. On the other hand, the generation of magnetism is always accompanied by spin splitting, which increases the overall energy of the system. The density of states of metal ions shifts toward the Fermi level, and the resulting additional unpaired electrons form a delocalized electron effect and enhance catalytic activity. This promotes electron transfer, which catalytically reduces the electrode reaction barrier and improves interfacial reaction kinetics. Regarding the regulation of reaction behavior at the aqueous electrode/electrolyte interface, Wang et al. introduced a delocalized electron catalytic strategy in the vanadium-based cathode, which could enhance desolvation and diffusion kinetics catalytically by constructing active sites on V_2O_5 cathode [11].

Inspired by this, we constructed an artificial SEI layer using magnetic spinel $ZnFe_2O_4$ nanoparticles (ZFO@Zn) on the surface of metallic Zn anode. The spinel structure provides three-dimensional (3D) channels for rapid Zn^{2+} diffusion [12]. Under an electric field, solvated $[Zn(H_2O)_6]^{2+}$ clusters are sieved by the channels, and abundant high-spin Fe^{3+} active sites provide delocalized electrons for achieving desolvation facilely. The free Zn^{2+} then travels uniformly along the micro paths to reach the metallic Zn surface for reduction and nucleation. During this process, the magnetic SEI layer modulates interfacial electric field distribution, suppressing disordered ion diffusion in the two-dimensional (2D) plane. Once the tip discharge phenomenon occurs with the central aggregation of the current in any region due to slight deposition differences, the micro-magnetic field deflects the current via the Lorentz force, eliminating dendrite growth tendencies and enabling long-term, self-limiting flat Zn deposition [13–16].

The superior performances of ZFO@Zn in interfacial reactions were confirmed by theoretical simulations and electrochemical testings. Through in-situ/ex-situ characterizations, we demonstrated that ZFO@Zn interface effectively suppresses surface corrosion and dendrite growth. The modified zinc anode maintained a low voltage hysteresis of 29 mV with a high reversibility of 99.02% for over 3000 h. Impressively, the anode stabilizes at an ultra-high current density of 30 mA cm^{-2} with only 147 mV polarization, delivering over 3500 mAh cm^{-2} cumulative capacity. Additionally, the ZFO interface could prevent the consumption of shuttling ions from vanadium-based cathodes, resulting in excellent capacity retention (90.7%, 3000 cycles) and low self-discharge rates (98.07%, 24 h) in the full cell with ZFO@Zn. To further validate this interface modification strategy, large-areal pouch cells assembled with ZFO@Zn exhibited stability for hundreds of operations and successfully charged for a smartphone, showcasing promising applications for next-generation energy storage systems.

2. Experimental section

2.1. Preparation of ZFO@Zn anode

The commercial $ZnFe_2O_4$ powder was combined with polyvinylidene fluoride (PVDF) in a ratio of 9:1 and mixed with *N*-methyl-2-pyrrolidone (NMP) under stirring to get a slurry. This slurry would be coated on the metallic Zn foil by using γ μm scraper (γ = 30, 50, 100, 200). The coated Zn foil dried in an oven at 60 °C for 6 h to evaporate all the solvents. Finally, the foils were cut to the desired sizes to obtain ZFO@Zn anode for testing.

2.2. Preparation of V_2O_{5-x} cathode

The fabrication of V_2O_{5-x} cathode is similar to our previous report. Briefly, commercial V_2O_5 was treated at 400 °C for 2 h under the 5% H_2/Ar atmosphere. The V_2O_{5-x} cathode was prepared by mixing V_2O_{5-x}, Super P, and PVDF in a ratio of 7:2:1 in NMP solvent to form a homogeneous slurry. This slurry was coated onto a carbon film, which was then cut into appropriate sizes. The average areal mass loading of the active material was approximately 1 mg cm^{-2}.

2.3. Fabrication of various cells

The coin cells for testing are assembled by using a glass fiber GF/B (Whatman) as separators in CR2025 coin cells. The Zn symmetric cells used 10 mm diameter Zn foils as electrodes. The 10 μm thick copper or titanium foils were cut into 15 mm diameter discs to serve as electrodes of half-cells. The 10 mm diameter V_2O_{5-x} cathodes and 12 mm diameter Zn foils are assembled as full cells. The 2 M $ZnSO_4$ was used as electrolyte for symmetric cells and half-cells, and 3 M $Zn(CF_3SO_3)_2$ for full cells.

2.4. Electrochemical measurements

All galvanostatic charge/discharge measurements were conducted on a battery testing instrument (Land CT2001A) at different current densities. All electrochemical tests were configured on a Biologic VMP-3 multichannel electrochemical workstation. Electrochemical impedance spectroscopy (EIS) measurements were performed in a frequency range of 200 kHz to 100 mHz at open circuit potential. Tafel curves were obtained using Zn symmetric cells with a voltage window from 0.2 V to −0.2 V at a scan rate of 1 mV s^{-1}. The ionic transference number was tested using Zn symmetric cells under a bias of 20 mV for 6000 s. Chronoamperometry (CA) curves were measured using Zn symmetric cells under a bias of 150 mV for 300 s. Linear sweep voltammetry (LSV) tests were conducted using a Zn//Ti half-cell at a scan rate of 1 mV s^{-1}. In-situ optical microscopy imaging was conducted using a commercial window electrochemical cell assembled with Zn symmetric cells for testing.

2.5. Material characterizations

The microstructure and elemental composition of the ZNB@Zn were examined using a field-emission scanning electron microscope (SEM, Hitachi Regulus 8230) and energy-dispersive spectroscopy (EDS, Quanta FEG 250). The crystalline phases were identified through X-ray diffraction (XRD) analysis performed on a Bruker AXS D8 Advance. X-ray photoelectron spectroscopy (XPS) analysis was carried out with an ESCALAB 250XI (Thermo Scientific) spectrometer to investigate the chemical states of the elements. Time-of-flight secondary-ion mass spectrometry (TOF-SIMS) was performed with a TOF-SIMS 5–100 system, using a 30 keV Bi^{3+} ion beam for sputtering to analyze the surface composition and depth profiles.

Distribution relaxation times (DRT) analysis was computed from EIS data by using an open-source Matlab toolbox of DRT tools, which was

developed by Professor Francesco Ciucci's research group [17–20]. The DRT tools is freely available from the following site: https://github.com/ciuccislab/DRTtools

2.6. Simulation method

The electronic structure and system energy calculations are performed based on density functional theory (DFT) implemented in the Vienna ab initio simulation package (VASP) [21,22] and Quantum ATK [23]. The spin polarization and spin-polarized DFT are used for $ZnFe_2O_4$ and $Zn_{1-x}Fe_{2+x}O_4$ systems, respectively. The exchange-correlation potential is explained by the Perdew-Burke-Ernzerhof (PBE) functional based on spin-generalized gradient approximation plus on-site Coulomb interaction (SGGA + U) functional [24,25] with U_{eff} = 3 eV on Fe−3*d* [26]. The projector augmented-wave method is used for wave function expansion with an energy cutoff of 450 eV. The geometry optimization continues until the energy differences and ionic forces converge to less than 10^{-6} eV and 0.01 eV/Å, respectively. Monk horst-Pack k-point meshes of 10× 10× 10 are used for electronic structure calculation of metal oxides (including Fe atom doping and Zn ion adsorption). Magnetic ground state energy tests of $ZnFe_2O_4$ and $Zn_{1-x}Fe_{2+x}O_4$ exhibit antiferromagnetism and ferrimagnetism, respectively. Calculation of desolvation energy barriers of $Zn(H_2O)_x^+$ into Zn $(H_2O)_{x-1}$ and $Zn(H_2O)_x^+$ on the different delocalization-electron catalyzers is set k-point meshes of 5 × 5 × 1. For the slab calculations, the vacuum thickness is 15 Å to reduce artificial interactions due to periodic boundary conditions.

3. Results and discussion

As illustrated in Fig. 1a, Zn^{2+} is encased in bulky solvated shells as $[Zn(H_2O)_6]^{2+}$ clusters, which hinder diffusion and introduce significant desolvation energy barriers [27,28]. This slows down the plating/

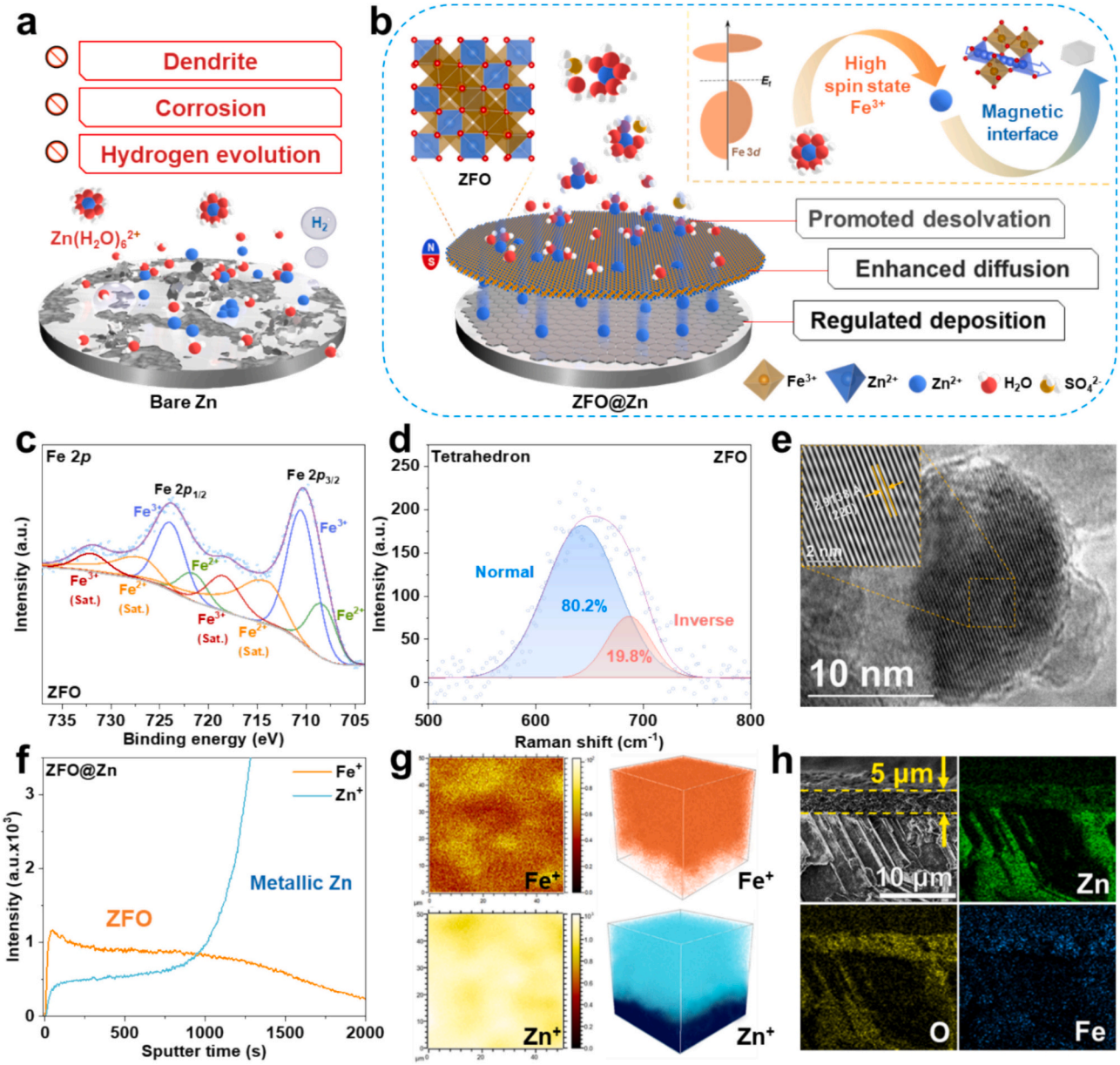

Fig. 1. Morphology and structural characterizations on ZFO artificial interfacial layer. (a) Challenges for metallic Zn anode. (b) Schematic illustration of the working mechanism of the ZFO layer. (c) High-resolution Fe 2*p* XPS spectrum of ZFO. (d) Raman spectrum of ZFO. (e) HR-TEM image and diffraction fringes of ZFO nanoparticles. (f) TOF-SIMS sputtering depth profiles. (g) 2D planar mappings and 3D reconstructions of ZFO@Zn anode. (h) Cross-sectional SEM image of ZFO@Zn and corresponding elemental mapping.

stripping process and leads to nonuniform deposition. The dissociation of hydrated $[Zn(H_2O)_6]^{2+}$ at the electrode/electrolyte interface releases highly reactive water molecules, exacerbating HER and surface corrosion. [8] The inert by-products from side reactions degrade interfacial conductivity with electron injection and perpetuate a vicious cycle [4]. These issues not only increase futile energy loss but also severely limit AZMBs reversibility and lifespan.

Zinc ferrite (ZFO) is a highly stable material characterized by its resistance to high temperature or corrosion, making it widely applicable across various fields. Its magnetic properties make it suitable for manufacturing electromagnetic devices. Also, its excellent electromagnetic shielding capability enables it to be used as a wave-absorbing material. With a theoretical specific capacity over three times that of graphite, ZFO has also been studied as an anode material for lithium-ion batteries. [29] As an n-type narrow-bandgap semiconductor, its photocatalytic activity and photoelectric conversion properties have garnered significant attention in related fields. Additionally, ZFO is cost-effective and easily obtained by separating it from zinc ore slag. In conclusion, constructing the artificial SEI layer by ZFO for Zn anode has great advantages and substantial commercialization prospects. As shown in Fig. 1b, the spinel-type ZFO exhibits a cubic crystal structure with *Fd3m* symmetry. In this structure, oxygen atoms form a face-centered cubic array at the 32e sites, while Zn and Fe atoms occupy the 8*a* tetrahedral and 16*d* octahedral sites, respectively. The unoccupied 16*c* sites form edge-sharing 3D channels with 8*a* sites, enabling rapid Zn^{2+} diffusion. These channels induce the pre-desolvation of hydrated Zn^{2+} by the sieving mechanism outside the SEI layer. Additionally, the high-spin Fe^{3+} metal centers provide abundant delocalized electrons that facilitate the charge transfer process and reduce desolvation and diffusion barriers, which catalytically promote the dissociation of solvated shell and transfer of free ions to achieve unimpeded Zn deposition.

The standard spinel-structured $[Zn]_A[Fe_2]_BO_4$ exhibits a net magnetic moment of zero due to the mutual cancellation of magnetic moments between Fe^{3+} in the octahedral sites, which makes itself paramagnetic. However, surface defects and cation disorder lead to Fe^{3+} partially occupying tetrahedral sites in nanoscale particles, forming a hybrid spinel structure of $[Zn_xFe_{1-x}]_A[Zn_{1-x}Fe_{1+x}]_BO_4$ with ferrimagnetic property [30]. This phenomenon is evidenced by the attraction of ZFO nanoparticles to a magnet and compass, as demonstrated in Fig. S1. To gain deeper insights into the origin of this magnetism, the valence states of the elements in ZFO were analyzed by using X-ray photoelectron spectroscopy (XPS). High-resolution XPS of Fe 2*p* (Fig. 1c) reveals a small amount of Fe^{2+} doping within the ZFO nanoparticles. To maintain charge balance, the O 1 *s* spectrum (Fig. S2) also displays a peak at 532.1 eV corresponding to oxygen vacancies. Raman spectra further support this observation, the peak above 600 cm^{-1} is attributed to the stretching vibrations of tetrahedral interstices. Since the radius of Zn^{2+} is larger than that of Fe^{3+}, the peaks at 650 cm^{-1} and 680 cm^{-1} are assigned to Zn^{2+} and Fe^{3+} occupying tetrahedral sites, respectively [31]. As shown in Fig. 1d, the tested ZFO nanoparticles consist of 80.2% normal spinel phase and 19.8% inverse spinel phase. X-ray diffraction (XRD) pattern (Fig. S3) confirms consistency with the reported $ZnFe_2O_4$ (PDF#79–1150), with a fitted lattice parameter of 8.406 Å, smaller than the 8.436 Å of normal spinel $ZnFe_2O_4$. This reduction is attributed to the tetrahedral sites of Fe^{3+} occupying a smaller radius, thereby decreasing atomic interactions. The presence of defects and atomic disorder in nanoscale crystals not only generates a net magnetic moment between Fe^{3+} ions, resulting in ferrimagnetism of ZFO, but also elevates the crystal field splitting energy of ZFO above the electron pairing energy. This causes the *d*-orbital occupation of Fe^{3+} to transition from a low-spin state (t_{2g}^5) to a high-spin state ($t_{2g}^3e_g^2$), increasing the number of unpaired electrons [32]. The enhanced electron exchange interactions between Fe^{3+} and polar water molecule ligands affect the coordination behavior and desolvation energy barrier of adjacent Zn^{2+} ions [33–36]. Vibrating sample magnetometer (VSM) result of ZFO powder (Fig. S4) reveals a saturation magnetization (Ms) of 21.59 emu g^{-1} and remanence (Br) of 2.03 emu g^{-1}, which confirms that the commercial nano ZFO is a soft ferrimagnetic material.

High-resolution transmission electron microscopy (HR-TEM) images (Fig. 1e and S5) reveal an average particle size of approximately 20 nm, enabling uniform coating on the Zn anode surface to construct an artificial SEI layer. The observed lattice fringes with a spacing of 0.291 nm correspond to the (220) planes of the spinel structure, which consist with previous conclusion of smaller crystal parameter.

In preliminary exploratory experiments, four scraper thicknesses were used to investigate the optimal preparation process for the artificial layer of ZFO zinc anode. As shown in Fig. S6, due to limitations in slurry viscosity and the surface flatness of Zn foil, the coating prepared with 30 μm scraper exhibited uneven distribution. Coatings fabricated using 50, 100, and 200 μm scrapers yielded thicknesses of 5, 9, and 15 μm, respectively. These coatings constructed a uniformly modified interface layer and exhibited a dense and smooth dark orange surface, indicating effective structural control. Symmetric cell tests were conducted on Zn anodes with ZFO artificial layers of varying thicknesses (Fig. S7). The ZFO@Zn prepared with the 50 μm scraper demonstrated the lowest overpotential, while the overpotential increased with greater thickness. Consequently, the 50 μm ZFO@Zn was selected for subsequent experiments and investigations.

To confirm the composition of ZFO layer, time-of-flight secondary ion mass spectrometry (TOF-SIMS) using Cs^+ sputtering was conducted (Fig. 1f). After 1200 s, the Fe^+ signal intensity decreased significantly, while Zn^+ content increased rapidly, indicating the presence of the ZFO layer. The 2D planar mappings and 3D reconstructions of Zn^+ and Fe^+ (Fig. 1g) further illustrate the uniform ZFO artificial layer on the metallic Zn anode surface. (Fig. 1h) The cross-sectional SEM image with related elemental mapping of the ZFO@Zn anode by energy-dispersive spectroscopy (EDS) corroborates the uniform distribution of ZFO layer. In conclusion, the successful construction of the ZFO artificial SEI layer is verified through these characterizations. Its appropriate thickness and uniform distribution are expected to facilitate the Zn plating/stripping process.

To elucidate the interaction mechanism between Zn^{2+} with the ZFO used in the experiments and thoroughly investigate their influence on interfacial reactions, density functional theory (DFT) simulations of ZFO materials were systematically analyzed. Through the electronic density of states (DOS) for two ZFO structures, it is evident that the hybrid type ZFO exhibits spin splitting in the electronic states dominated by high-spin Fe 3*d* valence orbitals due to Zn/Fe atomic disorder, which fundamentally explains its ferrimagnetic properties (Fig. 2a). Concurrently, the overall DOS shifts toward the Fermi level, indicating enhanced electron delocalization characteristics and superior electrochemical activity to facilitate reaction kinetics [37]. By constructing adsorption models on metallic Zn, standard ZFO, and hybrid ZFO surfaces, various adsorption sites were systematically selected to investigate Zn^{2+} adsorption mechanisms. As shown in Fig. 2b, the adsorption energy of Zn^{2+} on the bare Zn surface is −0.539 eV. The Zn top site on standard ZFO demonstrates a higher adsorption energy (−0.826 eV), with other sites lower than that of the bare Zn surface. Remarkably, the hybrid ZFO surface universally displays higher adsorption energies with the maximum value (−0.842 eV) observed at the hollow site, confirming its superior Zn^{2+} adsorption capability. Comparative analysis of charge density differences in optimal adsorption configurations (Fig. 2c) reveals that the hybridization of the high-spin e_g orbitals with O 2*p* orbitals reduces the energy level of these orbitals and then promotes preferential Zn^{2+} adsorption at Fe—O bridge sites. The Zn^{2+} diffusion barrier for different materials was calculated to evaluate their transport kinetics. As the simulation results demonstrate that hybrid ZFO possesses an ultra-low Zn^{2+} migration barrier of 0.099 eV, enabling rapid ion transport within the ZFO spinel framework (Fig. 2d). Furthermore, desolvation energy simulations reveal that hydrated Zn^{2+} requires overcoming a high energy barrier (4.544 eV) for water dissociation on bare Zn surfaces, which is a critical limitation for interfacial kinetics. In contrast,

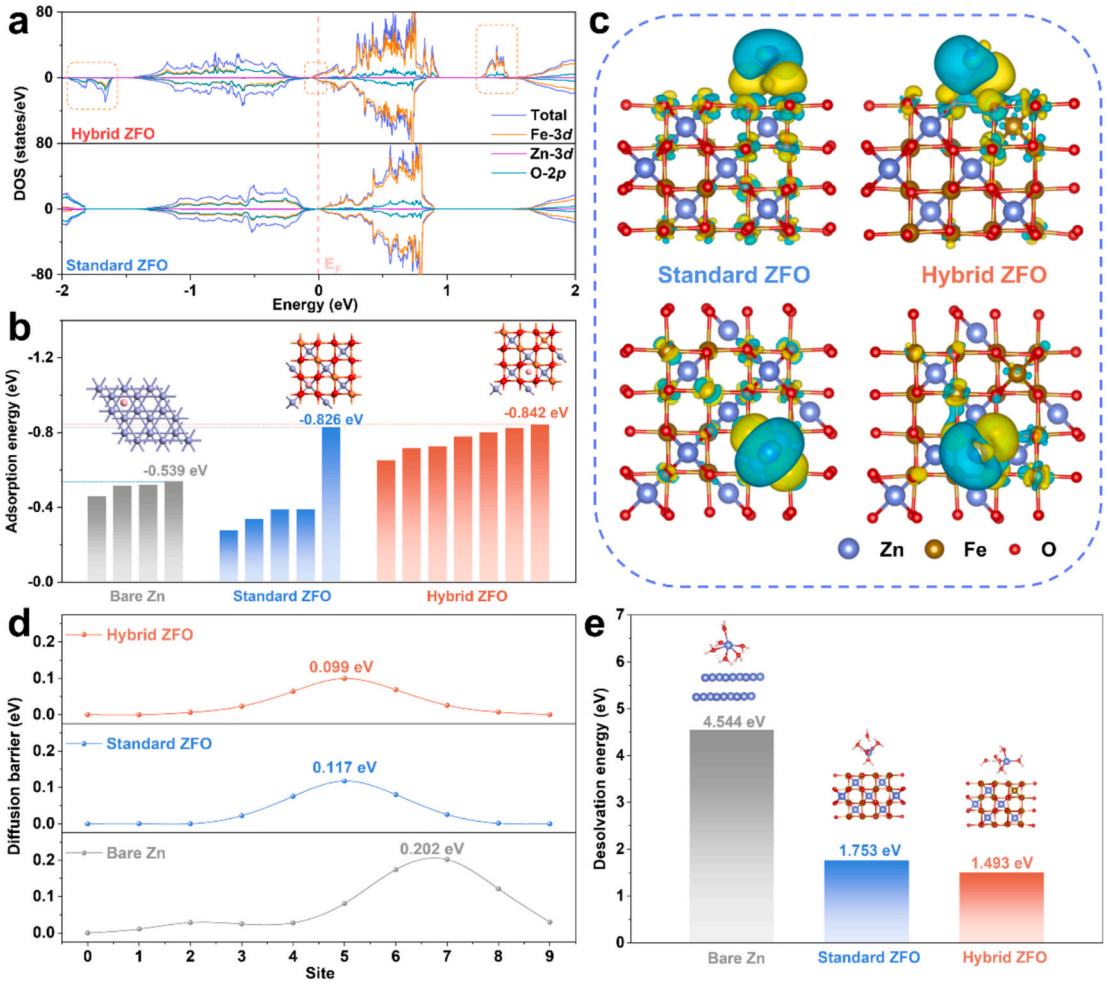

Fig. 2. DFT simulation of ZFO. (a) Density of states for two ZFO structures. (b) Adsorption energies of Zn^{2+} at various surface sites. (c) Charge density difference for Zn^{2+} adsorption on ZFO surfaces. (d) Diffusion energy barriers of Zn^{2+} across different surfaces. (e) Desolvation energy barriers of $Zn(H_2O)_6^{2+}$ on various surfaces.

the hybrid ZFO surface significantly reduces this barrier to 1.493 eV, demonstrating exceptional catalytic activity for desolvation processes (Fig. 2e). These computational insights collectively highlight the promising application potential of ZFO in advanced AZMBs.

The experimental results validated the simulation results. Since desolvation is identified as the rate-determining step in the charge transfer process, the activation energy (E_a) derived from calculating the charge transfer resistance (R_{ct}) at varying temperatures via the Arrhenius equation serves as a quantitative metric to evaluate the desolvation energy barrier (Fig. 3a and S8) [4]. The E_a for ZFO@Zn (21.23 kJ mol^{-1}) is markedly lower than that of bare Zn (36.28 kJ mol^{-1}). This substantial reduction demonstrates the ability of ZFO layer to enhance desolvation kinetics for $[Zn(H_2O)_6]^{2+}$ clusters.

Electrochemical impedance spectroscopy (EIS) analysis is a widely used method for probing electrode reaction kinetics. Its result reveals that the incorporation of the ZFO layer significantly reduces impedance (Fig. 3b). To further investigate the impact of the ZFO layer on deposition kinetics, the distribution of relaxation times (DRT) technique was applied to analyze the EIS data (Fig. 3c). The reduction in corresponding peaks indicates that the ZFO layer promotes all critical steps in zinc deposition, including adsorption, charge transfer, and diffusion. The high ionic conductivity of the ZFO layer enables rapid diffusion kinetics. Supporting this, EIS measurements of Ti symmetric cells reveal a significant reduction in ohmic resistance from 1.99 Ω (bare Ti) to 0.65 Ω (ZFO@Ti), demonstrating its exceptional facilitation for Zn^{2+} transport (Fig. S9). Consequently, ZFO@Zn exhibits a significantly higher ion transference number (0.449) in comparison with bare Zn (0.139) (Fig. 3d and S10). As shown in Fig. S11, the contact angle between the bare Zn anode and the electrolyte is 105.92°, while that of ZFO@Zn is significantly reduced to 51.13° due to ZFO's zincophilic properties and superior transport kinetics, which demonstrates excellent wettability and facilitates interfacial contact. To quantify the impact of the ZFO layer on Zn^{2+} deposition process, Zn//Cu asymmetric cells were assembled and tested by cyclic voltammetry (CV) method. The results (Fig. 3e) reveal that ZFO layer significantly reduces voltage hysteresis, and the enhanced peak current indicates the presence of more nucleation sites.

As a more in-depth view, this improvement stems from alterations in interfacial solvent structures. The solvation environment is shown by the Raman spectra of the OSO_3^{2-} bond region at 970–1000 cm^{-1} (Fig. 3f and S12). With increasing sulfate concentration, the free water content decreases, and the OSO_3^{2-} stretching vibration exhibits a blue shift, indicating a transition from solvent-separated ion pairs (SSIP, $[Zn^{2+}(H_2O)_6$ $OSO_3^{2-}]$) to contact ion pair (CIP, $[Zn^{2+}(H_2O)_5$ $OSO_3^{2-}]$). The higher CIP ratio on the ZFO@Zn surface (58.6%) suggests that Zn^{2+} can achieve a more readily desolvation process before entering the ion transport channels, which is facilitated by the sieving mechanism and electrons delocalization effect of ZFO layer. Further insights into activation of water with Raman spectra at 3000–3800 cm^{-1} region by the O – H stretching vibration (Fig. 3g and S13) show an increase in strong hydrogen bonds on the ZFO@Zn surface (from 54.1% for bare Zn to 71.2%). This is accompanied by decreases in medium and weak hydrogen bonds from 35.5% and 10.4% to 27.2% and 1.6%, respectively. It indicates the reduction in free active water content by the

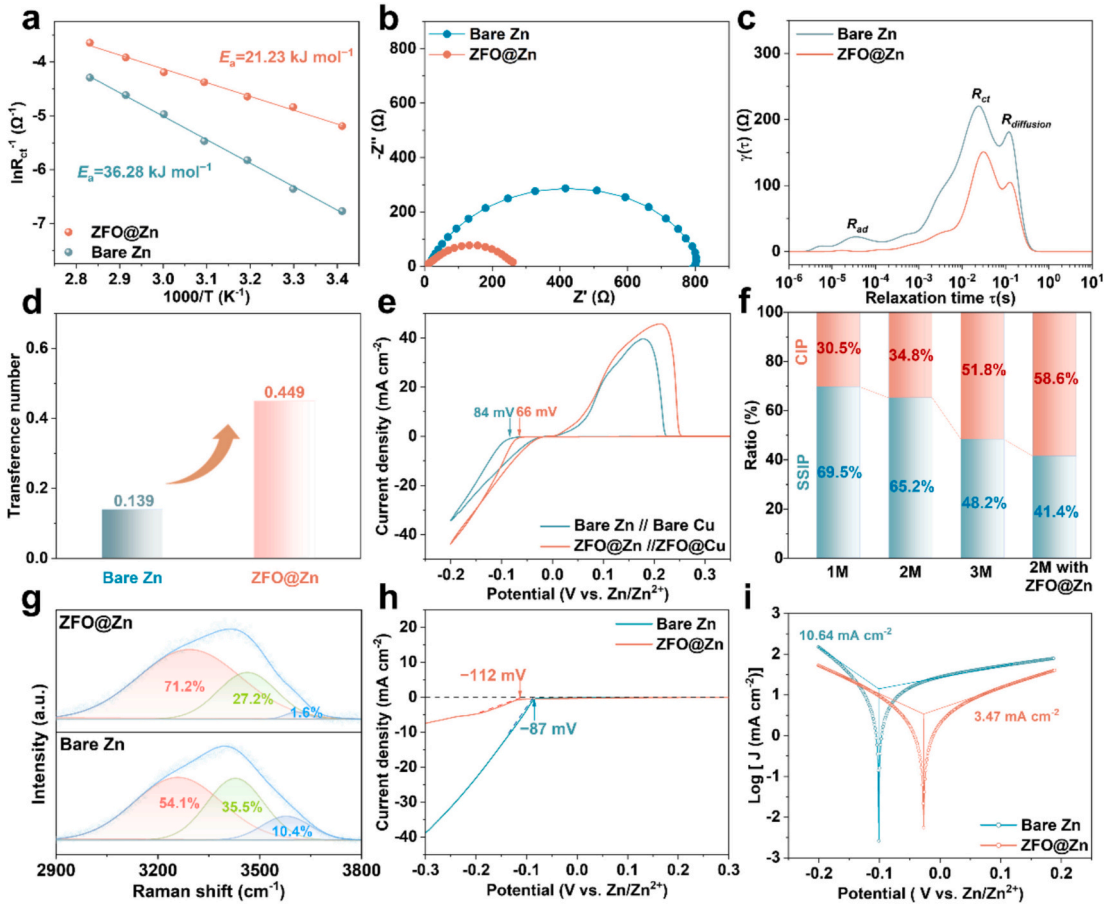

Fig. 3. Electrochemical characterization and interfacial spectroscopy. (a) Desolvation activation energy fitted for ZFO@Zn and bare Zn. (b) EIS analysis of ZFO@Zn and bare Zn symmetric cells. (c) DRT analysis and (d) ion transference numbers of ZFO@Zn and bare Zn anodes. (e) CV curves of Zn//Cu asymmetric cells. (f) Proportions of Zn^{2+}-OSO_3^{2-} ion pairs under different environments. (g) Raman spectra of OH bonds on ZFO@Zn and bare Zn surfaces. (h) LSV curves and (i) Tafel polarization curves of ZFO@Zn and bare Zn anodes.

modulation of the ZFO layer. Consequently, the associated HER and corrosion processes are also significantly mitigated.

Linear sweep voltammetry (LSV) results (Fig. 3h) reveal a higher HER onset potential for ZFO@Zn (112 mV) in comparison with bare Zn (87 mV), confirming its superior HER suppression. As the detection of Tafel polarization curves (Fig. 3i), the corrosion reaction rate on the Zn anode surface can be reflected by the slope of strongly polarized region, and the corrosion current density (I_{corr}) of bare Zn is approximately three times higher than that of ZFO@Zn (10.64 vs. 3.47 mA cm^{-2}), also confirming a significant reduction in corrosion reaction for ZFO@Zn [38].

Time-of-flight secondary ion mass spectrometry (TOF-SIMS) analysis (Fig. 4a) provides further insights into the post-cycling Zn anode. The top 2D planar mappings of ZnO^- reveal clustered deposits on bare Zn, and ZFO@Zn achieves uniform deposition. The appearance of dendritic protrusions on the bare Zn surface can be more visually seen on the 3D reconstructed image, and the distribution of $ZnOH^-$ and SO_3^- mutually corroborates its poor surface coverage by thick ZHS by-product. On the contrary, the Zn anode protected by the ZFO layer shows suppressed side reactions and compact zinc deposition.

The comparison of the XRD patterns between the Zn anode before and after cycling (Fig. 4b) further corroborates the above observation. Diffraction peaks at 2θ = 15–30 ° on cycled bare Zn correspond to the ZHS standard sample, indicating the existence of rampant side reactions on the bare Zn surface. The increased ratio of the 002/101 crystalline plane diffraction peak area on the ZFO@Zn surface then evidences the parallel-preferential nucleation-inducing ability of the ZFO artificial SEI layer.

In situ optical microscopy (Fig. 4c) recorded the changes in surface morphology during the deposition of bare Zn and ZFO@Zn, respectively. The bare Zn surface developed irregular protrusions within 10 min of deposition, which evolved into sharp dendrites by just 30 min. In contrast, the ZFO@Zn surface remained flat throughout the deposition process, highlighting the superior regulation ability of the ZFO layer over Zn deposition behavior. The cross-sectional SEM images of the post-cycling ZFO@Zn (Fig. S14) show the flat Zn deposition behavior under ZFO layer and sustain interfacial contact integrity even under a high current density of 10 mA cm^{-2}. SEM analysis from top view (Fig. 4d) confirms that ZFO@Zn promotes uniform planar deposition with 002 crystal phase nucleation, whereas bare Zn exhibits uneven, aggregated deposition with hexagonal ZHS by-products [39]. The chronoamperometric curve (Fig. 4e) demonstrates that the ZFO-modified Zn anode maintains a stable negative current plateau corresponding to dense Zn deposition, whereas the bare Zn exhibits an uncontrolled increase in current magnitude due to irregular dendritic growth.

Fig. 4f provides a clearer understanding of the mechanism by which the ZFO layer regulates zinc deposition behavior. For bare Zn anodes, dendrite growth is intrinsically related to tip-discharge effects. Uneven surfaces lead to disordered 2D diffusion and ion clustering. Fortunately, the magnetic SEI layer composed of ZFO effectively mitigates these issues. The micro-magnetic field generated by the ZFO layer reconstructs the disordered interfacial electric field. As previous studies have demonstrated, ion flux on the magnetic surface is redirected into a helical motion under the Lorentz force, suppressing tip-discharge effects.

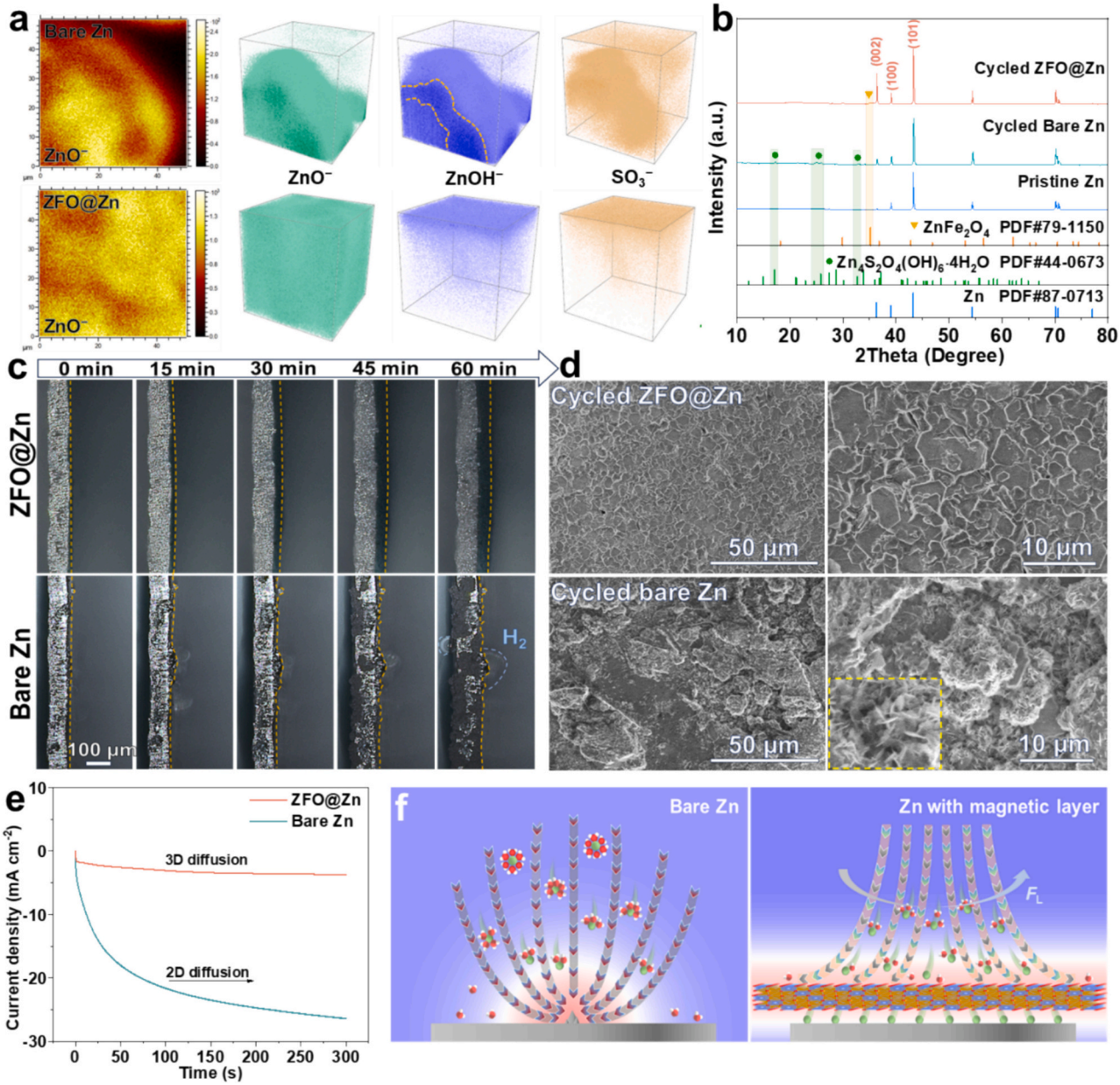

Fig. 4. Investigation of interfacial zinc deposition behavior. (a) Post-cycling 2D planar mappings and 3D reconstructions by TOF-SIMS for ZFO@Zn and bare Zn. (b) XRD patterns of Zn anodes before and after cycling. (c) In-situ optical microscopy of the deposition evolution of Zn surface morphology. (d) SEM surface morphologies of ZFO@Zn and bare Zn after cycling. (e) Chronoamperometry curves of ZFO@Zn and bare Zn anode. (f) Schematic illustration of Zn deposition regulated by the magnetic layer.

[10,14,40,41] The free Zn^{2+} travels through evenly distributed ion-conducting channels after desolvation, achieving stable 3D deposition and avoiding dendrite formation. The real-time simulations of electric field and ion concentration distributions during deposition on different Zn anode surfaces provide microscopic mechanistic evidence validating the aforementioned design by COMSOL Multiphysics software. As shown in Fig. S15, the bare Zn anode exhibited electric field aggregation due to the tip effect of surface protrusions, leading to continuous dendrite growth. Rapid ion consumption caused a significant increase in ion concentration gradients, and concentration polarization intensified during deposition. In contrast, the Zn anode with a magnetic ZFO artificial layer maintained uniform electric field and Zn^{2+} concentration distributions even with surface protrusions, revealing the effectiveness of magnetic regulation in controlling deposition behavior.

To assess the reversibility of ZFO@Zn, charge/discharge cycling tests were performed on the assembled Zn//Cu half-cells. During galvanostatic plating/stripping tests, the capacity-voltage profiles (Fig. 5a and S16) demonstrate lower polarization voltages for ZFO@Zn//ZFO@Cu cells (48.4 vs. 97.5 mV). Thanks to the anti-corrosion and dendrite-suppression capability of ZFO layer, the ZFO@Zn//ZFO@Cu cell sustained over 600 highly reversible cycles at 1 mA cm^{-2} for 1 mAh cm^{-2} Zn deposition, whereas the control group failed after 120 cycles due to CE degradation and short circuits (Fig. 5b).

The measurement of the average CE during 50 cycles of plating/stripping in Zn//Cu asymmetric cells after pre-deposition (Fig. 5c and S17) shows that ZFO@Zn//ZFO@Cu asymmetric cell achieved a CE of 99.02%, compared to 97.82% for the bare counterpart. The higher CE indicates that ZFO layer effectively suppresses side reactions with Zn consumption [42]. Galvanostatic intermittent titration tests (GITT) on Zn symmetric cells reveal reduced ohmic resistance and voltage

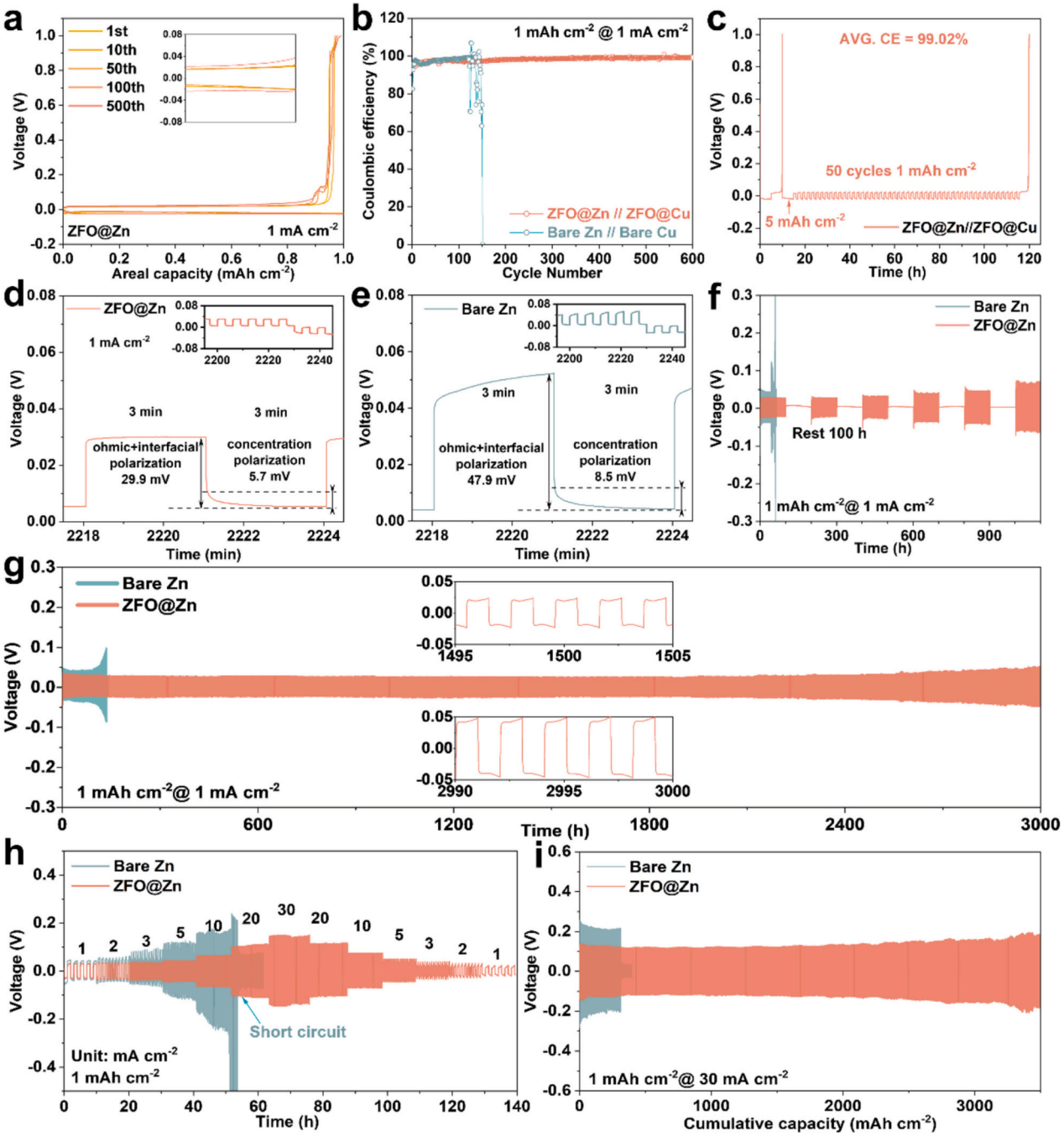

Fig. 5. Dendrite-free Zn plating performance with ZFO layer. (a) Capacity-voltage profiles and (b) cycling CE at 1 mA cm^{-2} for Zn//Cu asymmetric cells. (c) Voltage-time profiles for 50 cycles average CE of ZFO@Zn//ZFO@Cu. GITT curves for concentration polarization relaxation of (d) ZFO@Zn and (e) bare Zn symmetric cells. Voltage-time profiles of (f) resting-cycle and (g) long-term cycling stability for ZFO@Zn and bare Zn symmetric cells at 1 mA cm^{-2}. (h) Rate performance of ZFO@Zn and bare Zn symmetric cells. (i) Cycling stability of Zn symmetric cells at a high current density of 30 mA cm^{-2}.

polarization under the regulation of ZFO layer (Fig. 5d-e). Critically, it can investigate the concentration polarization hysteresis through time relaxation of a certain duration. ZFO@Zn displays significantly lower concentration polarization (5.7 mV) than bare Zn (8.5 mV), which is attributed to its fast desolvation and diffusion capabilities [43].

In prolonged rest experiments (Fig. 5f), bare Zn suffered severe passivation due to by-product accumulation, leading to extremely high polarization and cell failure after 50 cycles by hindered Zn deposition. In contrast, ZFO@Zn maintained interfacial stability through multiple rest periods. EIS tests during the cycling process (Fig. S18) show that ZFO@Zn symmetric cell consistently maintains a significantly lower impedance in comparison with the bare one during the first 50 cycles, highlighting the stable interfacial contact and enhanced electrode reaction kinetics. In symmetric cell tests at 1 mA cm^{-2} (Fig. 5g), ZFO@Zn exhibited outstanding long-term stability, sustaining low polarization (29 mV) over 3000 h, while bare Zn failed after only 130 h. In the rate performance test (Fig. 5h), a similar comparative trend is still detected, the ZFO@Zn anode demonstrates excellent low voltage polarization. As the current density increased from 1 mA cm^{-2} to 30 mA cm^{-2}, the ZFO@Zn symmetric cell maintained low voltage hysteresis of 29, 34, 37, 44, 62, 100, and 147 mV, respectively. In contrast, the bare Zn symmetric cell exhibited significantly higher voltage polarization and finally

short-circuited during this process. During continuous charging/discharging at an ultra-high current density of 30 mA cm^{-2} (Fig. 5i), the ZFO@Zn anode demonstrated a cumulative capacity of more than 3500 mAh cm^{-2}. The 40% depth of discharge (DOD) tests indicate that the bare Zn anode short-circuited after only a few cycles under high-voltage polarization due to dendrite formation, whereas ZFO@Zn maintained stable cycling for over 250 h under interfacial layer regulation (Fig. S19). ZFO modification strategy shows excellent cycling stability in comparison with recently reported inorganic artificial layers (Fig. S20 and Table S1). Overall, the performances of ZFO@Zn symmetric cell demonstrate an ultra-stable operation with low polarization, attributed to the exceptional corrosion resistance, rapid ion transport, and self-motivated deposition mechanism from the ZFO artificial SEI layer, further reinforcing the previously discussed findings.

To further verify the performance of the ZFO@Zn anode in practical application scenarios, we assembled a Zn//V_2O_{5-x} full cell for testing. The SEM images and corresponding EDS elemental mapping of the V_2O_{5-x} cathode are provided in Fig. S20. As expected, ZFO@Zn//V_2O_{5-x} exhibited significantly lower electrochemical impedance (Fig. 6a). The CV test of full cells reflects the cathode reaction behavior and kinetics, the two pairs of redox peaks in Fig. 6b correspond to the interconversion of V^{3+}/V^{4+} and V^{4+}/V^{5+} in the vanadium-based battery. From Fig. S21, there is a clear comparison that the voltage polarization between the V^{3+}/V^{4+} and V^{4+}/V^{5+} redox peaks of the ZFO@Zn//V_2O_{5-x} full cell decreased from 291 mV and 184 mV to 207 mV and 93 mV, respectively, which reveals the excellent ion transport ability of the ZFO layer. After a

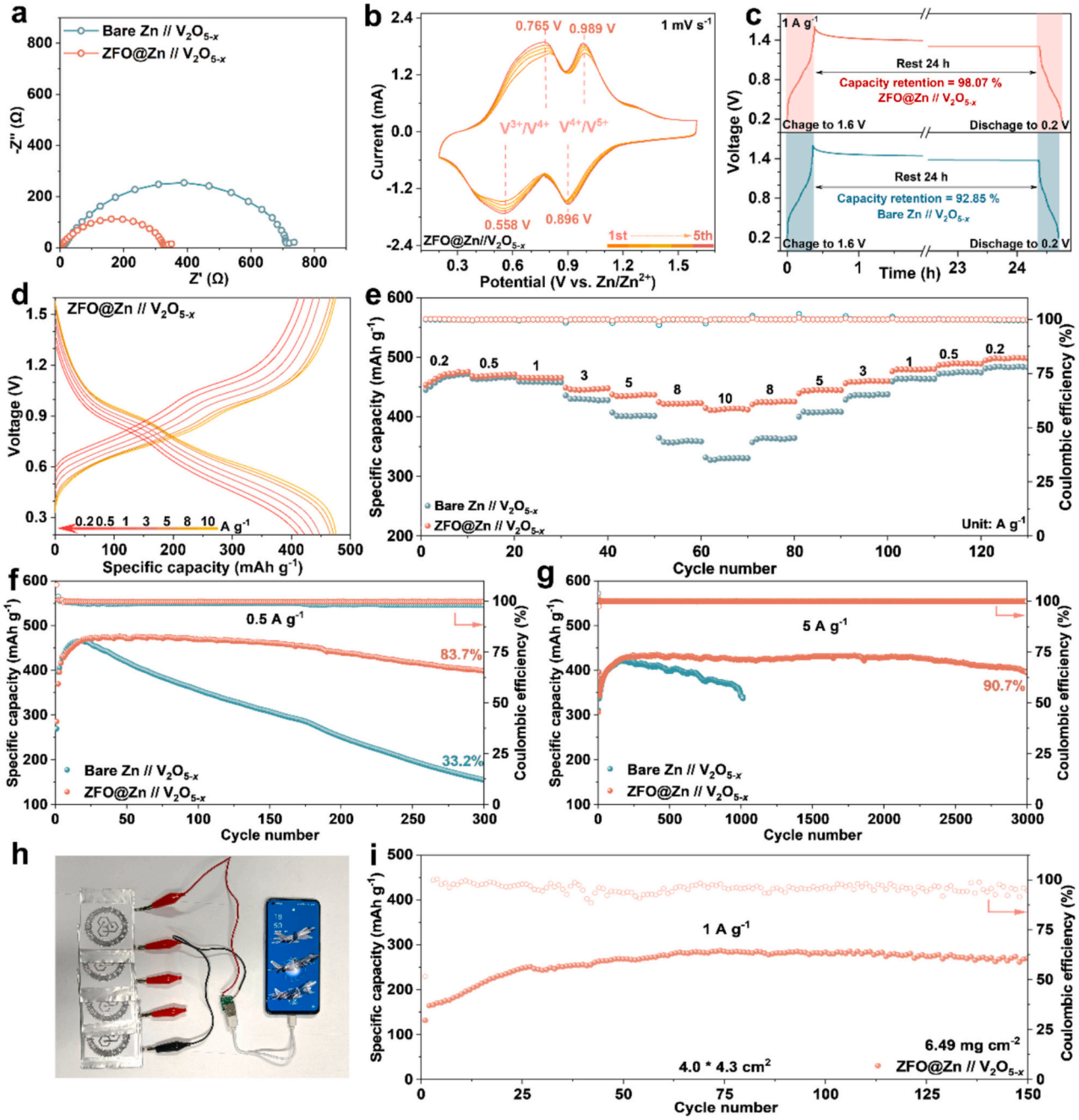

Fig. 6. Electrochemical performance of full batteries based on the ZFO@Zn anode. (a) EIS analysis, (b) CV curves and (c) self-discharge profiles of V_2O_{5-x} full cells. (d) Capacity-voltage curves of ZFO@Zn//V_2O_{5-x} at different current densities. (e) Rate performance of full cells. Cycling performance at (f) 0.5 A g^{-1} and (g) 5 A g^{-1} for V_2O_{5-x} full cells. (h) Digital images of ZFO@Zn//V_2O_{5-x} pouch cells powering for smartphone and (i) cycling performance.

self-discharge test with a duration of 24 h (Fig. 6c), the ZFO@Zn full cell retained 98.07% of its original capacity, outperforming the bare Zn (92.85%), indicating the effectiveness of ZFO layer in suppressing cross-talk side reactions [44].

As shown in the rate performance tests (Fig. 6d-e), when the current density increased from 0.2 A g^{-1} to 10 A g^{-1}, the specific capacity of ZFO@Zn//V_2O_{5-x} full cell only decreased slightly from 475.7 mAh g^{-1} to 411.1 mAh g^{-1}. In contrast, the bare Zn counterpart experienced a significant drop to 327.3 mAh g^{-1} (Fig. S21), highlighting the great ability of ZFO layer to enhance ion transport and diffusion under high current density. It is widely known that the dissolution of metal ions from the vanadium-based cathode would become pronounced at low current density. When dissolved ions shuttle to the Zn anode surface and are consumed by side reactions, a huge irreversible loss of cathode capacity is caused. [45,46] At a current density of 0.5 A g^{-1}, the specific capacity of bare Zn//V_2O_{5-x} full cell dropped precipitously to 157.3 mAh g^{-1} after 300 cycles, and ZFO@Zn//V_2O_{5-x} full cell maintained 83.7% capacity retention (Fig. 6f), demonstrating its effectiveness to isolate irreversible cross-talk side reactions with metallic Zn. Furthermore, post-cycled bare Zn and ZFO@Zn surfaces were characterized via XPS and TOF-SIMS analyses (Fig. S22). The results demonstrate significant suppression of vanadium-oxygen shuttle by-products on the ZFO@Zn surface in comparison with bare Zn, which further validates the previous hypothesis. When the current density increased to 5 A g^{-1} (Fig. 6g), the ZFO-protected cell achieved 3000 stable cycles with 90.7% retention, whereas the bare Zn full cell could only sustain around 1000 cycles with a reduced capacity of 341.6 mAh g^{-1} before short-circuiting. Thus, the fast ionic conduction properties and self-motivated mechanism of ZFO artificial SEI layer are well-validated by full cell applications.

The series-connected pouch cell array assembled with the ZFO@Zn anode and V_2O_{5-x} cathode successfully powered the smart device. With a high cathode areal loading of 6.49 mg cm^{-2}, the pouch cell maintained stable operation for 150 cycles at a current density of 1 A g^{-1}, achieving a high specific capacity of 288 mAh g^{-1}. This demonstrates the feasibility and advantage of the ZFO-coated anode modification strategy for future commercial applications.

4. Conclusions

In summary, zinc ferrate as a spinel-structured ferrimagnetic nanomaterial was proposed for the construction of artificial layers for AZMBs anodes. The 3D crystal structure and electron delocalization of ZFO layer enhance interfacial reaction kinetics, while its self-generated micro-magnetic field induces dendrite-free Zn deposition. Characterizations, simulations and electrochemical tests confirmed the excellent comprehensive properties of the ZFO layer, which enables the modified Zn anode to exhibit highly reversible long-cycle performance with low polarization. At a current density of 1 mA cm^{-2}, the ZFO@Zn anode sustained dendrite-free stable cycling for over 3000 h. Even under an ultrahigh current density of 30 mA cm^{-2}, it demonstrated a low voltage polarization of 147 mV and an impressive cumulative capacity of 3500 mAh cm^{-2}. Thanks to the inhibition of side reactions by ZFO layer, the ZFO@Zn//V_2O_{5-x} full cell maintained stable cycling for 3000 cycles at 5 A g^{-1} with a capacity retention rate of 90.7%. The simple preparation method and low cost of ZFO layer provide a promising pathway for the development and commercialization of high-performance AZMBs, expanding their practical applications and market potential.

CRediT authorship contribution statement

Haifeng Yang: Writing – review & editing, Writing – original draft, Visualization, Validation, Methodology, Investigation, Formal analysis, Data curation. **Fangqi Liu:** Visualization, Software, Methodology, Data curation. **Bixian Chen:** Visualization, Validation, Investigation, Formal analysis. **Xiaomin Cheng:** Methodology, Investigation, Funding acquisition. **Qinghua Guan:** Methodology, Formal analysis. **Jing Dong:** Methodology, Investigation. **Teng Li:** Writing – review & editing, Validation, Formal analysis. **Lujie Jia:** Supervision, Project administration, Funding acquisition. **Wenbin Wang:** Supervision, Resources. **Jing Zhang:** Resources, Investigation. **Jiqiang Jia:** Resources, Investigation. **Yongzheng Zhang:** Methodology, Investigation, Formal analysis. **Canhuang Li:** Methodology. **Yunjian Liu:** Writing – review & editing, Validation, Supervision, Resources, Project administration, Formal analysis. **Hongzhen Lin:** Writing – review & editing, Validation, Supervision, Resources, Project administration, Funding acquisition, Data curation, Conceptualization. **Jian Wang:** Writing – review & editing, Supervision, Project administration, Methodology, Funding acquisition, Conceptualization.

Declaration of competing interest

The authors declare that they have no known competing financial interests or personal relationships that could have appeared to influence the work reported in this paper.

Acknowledgements

Dr. J. Wang thanks the fellowship funding provided by the Alexander von Humboldt Foundation. We acknowledge the National Key Research and Development Program of China (2021YFA1201503), the National Natural Science Foundation of China (21972164, 22279161, 12264038, 22309144), the Natural Science Foundation of Jiangsu Province (BK. 20210130), China Postdoctoral Science Foundation (Nos. 2023M732561 and 2024M762318), the Opening funding from Key Laboratory of Engineering Dielectrics and Its Application (Harbin University of Science and Technology) (No. KFM202507, Ministry of Education), and Suzhou Science and Technology Plan projects (SYC2022057) as well as the technical support from Nano-X, Suzhou Institute of Nano-tech and Nano-bionics, Chinese Academy of Sciences. We are sincerely grateful to Dr. Jiqiang Jia from the Advanced Materials Analysis and Test Center of Xi'an University of Technology for the analysis and discussion of electronic microscopy.

Appendix A. Supplementary data

Supplementary data to this article can be found online at https://doi.org/10.1016/j.cej.2025.164989.

Data availability

Data will be made available on request.

References

[1] Y. Dai, R. Lu, C. Zhang, J. Li, Y. Yuan, Y. Mao, C. Ye, Z. Cai, J. Zhu, J. Li, R. Yu, L. Cui, S. Zhao, Q. An, G. He, G.I.N. Waterhouse, P.R. Shearing, Y. Ren, J. Lu, K. Amine, Z. Wang, L. Mai, Zn^{2+}-mediated catalysis for fast-charging aqueous Zn-ion batteries, Nat. Catal. 7 (2024) 776–784, https://doi.org/10.1038/s41929-024-01169-6.

[2] C. Li, X. Cheng, Y. Zhang, J. Zhu, H. Zhou, Y. Yang, J. Xu, J. Wang, Y. Wang, H. Yu, C. Shen, L. Zhan, L. Ling, Towards low-temperature dendrite-free zinc anode by constructing functional MXene buffer layer with duplex zincophilic sites, J. Colloid Interface Sci. 671 (2024) 505–515, https://doi.org/10.1016/j.jcis.2024.05.202.

[3] M. Qiu, P. Sun, K. Han, Z. Pang, J. Du, J. Li, J. Chen, Z.L. Wang, W. Mai, Tailoring water structure with high-tetrahedral-entropy for antifreezing electrolytes and energy storage at −80 °C, Nat. Commun. 14 (2023), https://doi.org/10.1038/s41467-023-36198-5.

[4] L. Jia, H. Hu, X. Cheng, H. Dong, H. Li, Y. Zhang, H. Zhang, X. Zhao, C. Li, J. Zhang, H. Lin, J. Wang, Toward low-temperature zinc-ion batteries: strategy, progress, and prospect in vanadium-based cathodes, Adv. Energy Mater. 14 (2024), https://doi.org/10.1002/aenm.202304010, 2304010.

[5] L. Jiang, S. Han, Y. Hu, Y. Yang, Y. Lu, Y. Lu, J. Zhao, L. Chen, Y. Hu, Rational design of anti-freezing electrolytes for extremely low-temperature aqueous batteries, Nat. Energy 9 (2024) 839–848, https://doi.org/10.1038/s41560-024-01527-5.

[6] L. Zheng, H. Li, M. Gao, K. Huang, J. Wang, L. Su, L. Li, H. Lin, X. Gao, Z. Liu, H. Zhang, Screening ammonium-based cationic additives to regulate interfacial chemistry for aqueous ultra-stable Zn metal anode, Adv. Sci. 11 (2024), https://doi.org/10.1002/advs.202407102, 2407102.

[7] L. Yuan, J. Hao, C. Kao, C. Wu, H. Liu, S. Dou, S. Qiao, L. Yuan, Regulation methods for the Zn/electrolyte interphase and the effectiveness evaluation in aqueous Zn-ion batteries, Energ. Environ. Sci. 14 (2021) 5669–5689, https://doi.org/10.1039/D1EE02021H.

[8] X. Cheng, Y. Zuo, Y. Zhang, X. Zhao, L. Jia, J. Zhang, X. Li, Z. Wu, J. Wang, H. Lin, Superfast zincophilic ion conductor enables rapid interfacial desolvation kinetics for low-temperature zinc metal batteries, Adv. Sci. 11 (2024), https://doi.org/10.1002/advs.202401629, 2401629.

[9] Z. Wu, Y. Zuo, Y. Zhang, X. Li, J. Zhang, Y. Wang, C. Shen, X. Cheng, M. Liu, H. Liu, H. Lin, J. Wang, L. Zhan, L. Ling, Modulating inner Helmholtz layer by electrocatalytically sieving $[Zn(H_2O)^6]^{2+}$ for 10000-cycle zinc-ion hybrid capacitors under extremely harsh conditions, Energy Storage Mater. 70 (2024) 103463, https://doi.org/10.1016/j.ensm.2024.103463.

[10] S. Zhou, X. Meng, C. Fu, J. Chen, Y. Chen, D. Xu, S. Lin, C. Han, Z. Chang, A. Pan, Lithiophilic magnetic host facilitates target-deposited lithium for practical lithium-metal batteries, Small 19 (2023), https://doi.org/10.1002/smll.202207764, 2207764.

[11] J. Wang, H. Hu, L. Jia, J. Zhang, Q. Zhuang, L. Li, Y. Zhang, D. Wang, Q. Guan, H. Hu, M. Liu, L. Zhan, H. Adenusi, S. Passerini, H. Lin, Fast interfacial electrocatalytic desolvation enabling low-temperature and long-cycle-life aqueous Zn batteries, InfoMat 6 (2024) e12558, https://doi.org/10.1002/inf2.12558.

[12] S. Zhu, X. Wang, J. Le, N. An, J. Li, D. Liu, Y. Kuang, Striking stabilization effect of spinel cobalt oxide oxygen evolution electrocatalysts in neutral pH by dual-sites iron incorporation, Energy Environ. Mater. 7 (2024) e12594, https://doi.org/10.1002/eem2.12594.

[13] C.Y. Zhang, C. Zhang, G.W. Sun, J.L. Pan, L. Gong, G.Z. Sun, J.J. Biendicho, L. Balcells, X.L. Fan, J.R. Morante, J.Y. Zhou, A. Cabot, Spin effect to promote reaction kinetics and overall performance of lithium-sulfur batteries under external magnetic field, Angew. Chem. Int. Ed. 134 (2022) e202211570, https://doi.org/10.1002/ange.202211570.

[14] C. Sun, W. Zhang, D. Qiu, M. Tong, Z. Chen, S. Sun, C. Lai, Y. Hou, Practicable Zn metal batteries enabled by ultrastable ferromagnetic interface, Sci. Bull. 68 (2023) 2750–2759, https://doi.org/10.1016/j.scib.2023.08.063.

[15] Y. Zhang, H. Zheng, X. Tong, H. Zhuo, W. Yang, Y. Chen, G. Shi, Z. Chen, L. Zhong, X. Peng, Amphoteric supramolecular nanofiber separator for high-performance sodium-ion batteries, Energy Environ. Mater. 7 (2024) e12735, https://doi.org/10.1002/eem2.12735.

[16] Q. Wu, Y. Zhong, R. Chen, G. Ling, X. Wang, Y. Shen, C. Hao, Cu-Ag-C@Ni3S4 with core shell structure and rose derived carbon electrode materials: an environmentally friendly supercapacitor with high energy and power density, Ind. Crop Prod. 222 (2024) 119676, https://doi.org/10.1016/j.indcrop.2024.119676.

[17] J. Liu, T.H. Wan, F. Ciucci, A Bayesian view on the Hilbert transform and the Kramers-Kronig transform of electrochemical impedance data: probabilistic estimates and quality scores, Electrochim. Acta 357 (2020) 136864, https://doi.org/10.1016/j.electacta.2020.136864.

[18] F. Ciucci, C. Chen, Analysis of electrochemical impedance spectroscopy data using the distribution of relaxation times: a Bayesian and hierarchical Bayesian approach, Electrochim. Acta 167 (2015) 439–454, https://doi.org/10.1016/j.electacta.2015.03.123.

[19] M.B. Effat, F. Ciucci, Bayesian and hierarchical Bayesian based regularization for Deconvolving the distribution of relaxation times from electrochemical impedance spectroscopy data, Electrochim. Acta 247 (2017) 1117–1129, https://doi.org/10.1016/j.electacta.2017.07.050.

[20] T.H. Wan, M. Saccoccio, C. Chen, F. Ciucci, Influence of the discretization methods on the distribution of relaxation times deconvolution: implementing radial basis functions with DRTtools, Electrochim. Acta 184 (2015) 483–499, https://doi.org/10.1016/j.electacta.2015.09.097.

[21] G. Kresse, J. Hafner, Ab initio molecular dynamics for liquid metals, Phys. Rev. B. 47 (1993) 558–561, https://doi.org/10.1103/PhysRevB.47.558.

[22] G. Kresse, J. Furthmüller, Efficient iterative schemes for ab initio total-energy calculations using a plane-wave basis set, Phys. Rev. B 54 (1996) 11169–11186, https://doi.org/10.1103/PhysRevB.54.11169.

[23] S. Smidstrup, T. Markussen, P. Vancraeyveld, J. Wellendorff, J. Schneider, T. Gunst, B. Verstichel, D. Stradi, P.A. Khomyakov, U.G. Vej-Hansen, M.-E. Lee, S. T. Chill, F. Rasmussen, G. Penazzi, F. Corsetti, A. Ojanperä, K. Jensen, M.L. N. Palsgaard, U. Martinez, A. Blom, M. Brandbyge, K. Stokbro, QuantumATK: an integrated platform of electronic and atomic-scale modelling tools, J. Phys. Math. 32 (2019) 015901, https://doi.org/10.1088/1361-648x/ab4007.

[24] P. Haas, F. Tran, P. Blaha, K. Schwarz, Construction of an optimal GGA functional for molecules and solids, Phys. Rev. B. 83 (2011) 205117, https://doi.org/10.1103/PhysRevB.83.205117.

[25] M. Li, L. Chen, L. Gui, S. Cao, D. Liu, G. Zhao, M. Ding, J. Yan, D. Wang, Born–Oppenheimer molecular dynamics simulations on structures of high-density and low-density water: a comparison of the SCAN meta-GGA and PBE GGA functionals, Phys. Chem. Chem. Phys. 23 (2021) 2298–2304, https://doi.org/10.1039/D0CP05707J.

[26] Z. Shen, X. Jin, J. Tian, M. Li, Y. Yuan, S. Zhang, S. Fang, X. Fan, W. Xu, H. Lu, J. Lu, H. Zhang, Cation-doped ZnS catalysts for polysulfide conversion in lithium–sulfur batteries, Nat. Catal. 5 (2022) 555–563, https://doi.org/10.1038/s41929-022-00804-4.

[27] J. Wang, J. Zhang, J. Wu, M. Huang, L. Jia, L. Li, Y. Zhang, H. Hu, F. Liu, Q. Guan, M. Liu, H. Adenusi, H. Lin, S. Passerini, Interfacial "single-atom-in-defects" catalysts accelerating Li^+ desolvation kinetics for long-lifespan lithium-metal batteries, Adv. Mater. 35 (2023) 2302828, https://doi.org/10.1002/adma.202302828.

[28] Q. Guan, J. Wang, Q. Zhuang, J. Zhang, L. Li, L. Jia, Y. Zhang, H. Hu, H. Hu, S. Cheng, H. Zhang, H. Li, M. Liu, S. Wang, H. Lin, Q. Guan, Self-tandem catalysis of fast Mg^{2+} desolvation and sulfur conversions for ultrahigh-performance Mg–S batteries via serially-assembled atomic reactors, Energ. Environ. Sci. 17 (2024) 3765–3775, https://doi.org/10.1039/D3EE04028C.

[29] J. Li, Q. Meng, Y. Zhang, L. Peng, G. Yu, A.C. Marschilok, L. Wu, D. Su, K. J. Takeuchi, E.S. Takeuchi, Y. Zhu, E.A. Stach, Size-dependent kinetics during non-equilibrium lithiation of nano-sized zinc ferrite, Nat. Commun. 10 (2019), https://doi.org/10.1038/s41467-018-07831-5.

[30] M. Bohra, V. Alman, R. Arras, Nanostructured $ZnFe_2O_4$: an exotic energy material, Nanomaterials 11 (2021) 1286, https://doi.org/10.3390/nano11051286.

[31] N. Romčević, R. Kostić, M. Romčević, B. Hadžić, I. Kuryliszyn-Kudelska, W. Dobrowolski, U. Narkiewicz, D. Sibera, Raman scattering from ZnO (Fe) nanoparticles, Acta Phy. Pol. A. 114 (2008) 1323–1328.

[32] J. Philip, G. Gnanaprakash, G. Panneerselvam, M. Antony, T. Jayakumar, B. Raj, Effect of thermal annealing under vacuum on the crystal structure, size, and magnetic properties of $ZnFe_2O_4$ nanoparticles, J. Appl. Phys. 102 (2007).

[33] W. Gao, R. Peng, Y. Yang, X. Zhao, C. Cui, X. Su, W. Qin, Y. Dai, Y. Ma, H. Liu, Y. Sang, Electron spin polarization-enhanced Photoinduced charge separation in ferromagnetic $ZnFe_2O_4$, ACS Energy Lett. 6 (2021) 2129–2137, https://doi.org/10.1021/acsenergylett.1c00682.

[34] Y. Zhang, Z. Cao, S. Liu, Z. Du, Y. Cui, J. Gu, Y. Shi, B. Li, S. Yang, Charge-enriched strategy based on MXene-based polypyrrole layers toward dendrite-free zinc metal anodes, Adv. Energy Mater. 12 (2022), https://doi.org/10.1002/aenm.202103979, 2103979.

[35] C.Y. Zhang, X. Lu, X. Han, J. Yu, C. Zhang, C. Huang, L. Balcells, A.G. Manjón, J. Jacas Biendicho, J. Li, J. Arbiol, G. Sun, J.Y. Zhou, A. Cabot, Identifying the role of the cationic geometric configuration in spinel catalysts for polysulfide conversion in sodium–sulfur batteries, J. Am. Chem. Soc. 145 (2023) 18992–19004, https://doi.org/10.1021/jacs.3c06288.

[36] Y. Wang, W. Xu, Y. Zhang, C. Zeng, W. Zhang, L. Fu, M. Sun, Y. Wu, J. Hao, W. Zhong, Y. Du, R. Yang, Introducing spin polarization into mixed-dimensional Van der Waals Heterostructures for high-efficiency visible-light Photocatalysis, Energy Environ. Mater. 6 (2023) e12390, https://doi.org/10.1002/eem2.12390.

[37] J. Zhang, L. Pan, L. Jia, J. Dong, C. You, C. Han, N. Tian, X. Cheng, B. Tang, Q. Guan, Y. Zhang, B. Deng, L. Lei, M. Liu, H. Lin, J. Wang, Delocalized Electron engineering of MXene-immobilized atomic catalysts toward fast Desolvation and dendritic inhibition for low-temperature Zn metal batteries, Nano Lett. 25 (2025) 3756–3765, https://doi.org/10.1021/acs.nanolett.4c05503.

[38] X. Yu, Z. Li, X. Wu, H. Zhang, Q. Zhao, H. Liang, H. Wang, D. Chao, F. Wang, Y. Qiao, H. Zhou, S.-G. Sun, Ten concerns of Zn metal anode for rechargeable aqueous zinc batteries, Joule 7 (2023) 1145–1175, https://doi.org/10.1016/j.joule.2023.05.004.

[39] Z. Xiang, Y. Qiu, X. Guo, K. Qi, Z.-L. Xu, B.Y. Xia, Inherited construction of porous zinc hydroxide sulfate layer for stable dendrite-free Zn anode, Energ. Environ. Sci. 17 (2024) 3409–3418, https://doi.org/10.1039/D4EE00721B.

[40] M. Zhu, Y. Wang, Y. Wu, J. Liu, J. Zhang, H. Huang, X. Zheng, J. Shen, R. Zhao, W. Zhou, S. Wang, Greatly enhanced methanol oxidation reaction of CoPt truncated octahedral nanoparticles by external magnetic fields, Energy Environ. Mater. 6 (2023) e12403, https://doi.org/10.1002/eem2.12403.

[41] W. Yang, J. Xia, F. Shang, G. Yang, B. Wang, H. Cai, L. Jing, H. Zhu, S. Yang, C. Liang, G. Shao, Boosting peroxymonosulfate activation via co-based LDH-derived magnetic catalysts: a dynamic and static state assessment of efficient radical-assisted electron transfer processes, Energy Environ. Mater. 7 (2024) e12701, https://doi.org/10.1002/eem2.12701.

[42] J. Xiao, Q. Li, Y. Bi, M. Cai, B. Dunn, T. Glossmann, J. Liu, T. Osaka, R. Sugiura, B. Wu, J. Yang, J. Zhang, M.S. Whittingham, Understanding and applying coulombic efficiency in lithium metal batteries, Nat. Energy 5 (2020) 561–568, https://doi.org/10.1038/s41560-020-0648-z.

[43] L. Wang, B. Zhang, W. Zhou, Z. Zhao, X. Liu, R. Zhao, Z. Sun, H. Li, X. Wang, T. Zhang, H. Jin, W. Li, A. Elzatahry, Y. Hassan, H.J. Fan, D. Zhao, D. Chao, Tandem chemistry with Janus Mesopores accelerator for efficient aqueous batteries, J. Am. Chem. Soc. 146 (2024) 6199–6208, https://doi.org/10.1021/jacs.3c14019.

[44] H. Wang, A. Zhou, Z. Hu, X. Hu, F. Zhang, Z. Song, Y. Huang, Y. Cui, Y. Cui, L. Li, F. Wu, R. Chen, Toward simultaneous dense zinc deposition and broken side-reaction loops in the $Zn//V_2O_5$ system, Angew. Chem. Int. Ed. 63 (2024) e202318928, https://doi.org/10.1002/anie.202318928.

[45] X. Wang, A. Naveed, T. Zeng, T. Wan, H. Zhang, Y. Zhou, A. Dou, M. Su, Y. Liu, D. Chu, Sodium ion stabilized ammonium vanadate as a high-performance aqueous zinc-ion battery cathode, Chem. Eng. J. 446 (2022) 137090, https://doi.org/10.1016/j.cej.2022.137090.

[46] X. Wang, Y. Wang, A. Naveed, G. Li, H. Zhang, Y. Zhou, A. Dou, M. Su, Y. Liu, R. Guo, C.C. Li, Magnesium ion doping and micro-structural engineering assist $NH_4V_4O_{10}$ as a high-performance aqueous zinc ion battery cathode, Adv. Funct. Mater. 33 (2023) 2306205, https://doi.org/10.1002/adfm.202306205.